Materials Synthesis

DOI: 10.1002/anie.201403223

Synthesis and Properties of Lanthanide Ruthenium(III) Oxide Perovskites**

*Alexandra Sinclair, Jennifer A. Rodgers, Craig V. Topping, Martin Míšek, Ross D. Stewart, Winfried Kockelmann, Jan-Willem G. Bos, and J. Paul Attfield**

Abstract: *An extensive series of new $LnRuO_3$ perovskites has been synthesized at high pressure. These ruthenium(III)-based oxides are ruthenium deficient, and high-pressure samples have compositions close to $LnRu_{0.9}O_3$. These phases stabilize ruthenium(III) which is very unusual in oxides. X-ray and neutron powder diffraction studies show that the materials adopt orthorhombic perovskite superstructures in which the RuO_6 octahedra are tetragonally compressed. These distortions, and the Mott insulator properties of the materials, are driven by strong spin-orbit coupling.*

Ruthenium–oxide perovskites and related materials have a wide range of unusual electronic and magnetic properties,[1] for example spin-triplet superconductivity in Sr_2RuO_4,[2] magnetic-field-induced quantum criticality in $Sr_3Ru_2O_7$,[3] band ferromagnetism in $SrRuO_3$,[4] and localized magnetism in Ca_2RuO_4.[5] Ruthenium usually adopts oxidation states between +4 and +7 in oxides. Ruthenium(IV) is very common, for example RuO_2, the perovskites $ARuO_3$ (A = Pb, Ca, Sr, and Ba),[4,6,7] Ruddlesden–Popper materials $A_{n-1}Ru_nO_{3n+1}$ (A = Ca, Sr; n = 1–3), and $Ln_2Ru_2O_7$ pyrochlores for lanthanides Ln.[8] Ruthenium(V) is also found in many oxides, such as the double perovskites Ln_2LiRuO_6,[9] the ruthenocuprate superconductors $RuSr_2(Ln,Ce)_2Cu_2O_{10}$,[10] and pyrochlores $A_2Ru_2O_7$ (A = Cd, Hg).[11,12] The hexagonal perovskite $Ba_3NaRu_2O_9$ contains ordered ruthenium(V) and ruthenium(VI) states,[13] and $KRuO_4$ is an example of a ruthenium(VII) oxide.[14] In contrast, oxides of ruthenium in the +2 and +3 states are almost unknown, although a disordered ruthenium(II) oxide $SrFe_{0.5}Ru_{0.5}O_2$ was recently synthesized by the topochemical reduction of $SrFe_{0.5}Ru_{0.5}O_3$.[15] Herein, we report the syntheses, X-ray and neutron powder diffraction studies, and magnetic properties of a new series of simple ruthenium(III) oxides, the $LnRuO_3$ perovskites.

Although no structurally characterized ruthenium(III) oxides are known, there are several reports of $LaRuO_3$ and $PrRuO_3$. The synthesis and potential oxidation catalytic activity of $LaRuO_3$ was reported but the material was not structurally characterized.[16,17] Preparation of $PrRuO_3$ was described at 5 GPa pressure and 1400 °C, although an attempt to prepare $NdRuO_3$ under the same conditions yielded the pyrochlore $Nd_2Ru_2O_7$.[18,19] No other $LnRuO_3$ materials have been reported.

We have synthesized a series of $LnRuO_3$ perovskites, in which Ln = La, Pr, Nd, Sm, Eu, Gd, Tb, Dy, Ho, and Y, as polycrystalline powders, with X-ray diffraction patterns as shown in Figure 1. Perovskite $LaRuO_3$ was found to be accessible at ambient pressure; a stoichiometric mixture of dried La_2O_3 and RuO_2 was heated twice for 12 h at 1150 °C under N_2 gas, yielding 0.75 g of a single-phase $LaRuO_3$ perovskite. However, high pressures were needed to prepare the other $LnRuO_3$ materials, with the highest purity samples obtained at 10–11 GPa. The materials shown were prepared

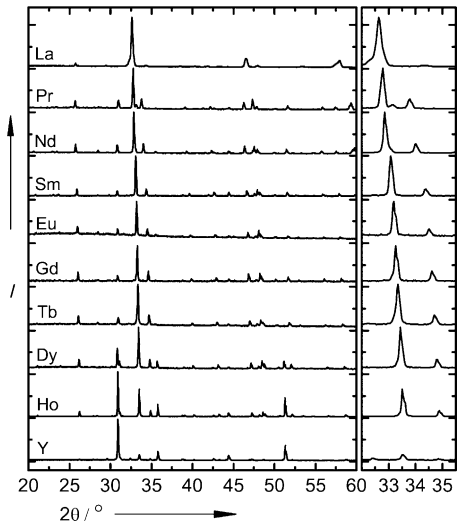

Figure 1. Powder X-ray diffraction patterns of $LnRuO_3$ samples using Cu Kα as the radiation source. The most intense peak of the perovskite is expanded at the right. The $2\theta = 31°$ peak is attributed to the $Ln_2Ru_2O_7$ pyrochlore in Ln = Dy, Ho, and Y samples. Rietveld powder data fitting analysis to these data are shown in the Supporting Information.

[*] Dr. A. Sinclair, Dr. J. A. Rodgers, C. V. Topping, Dr. M. Míšek, Prof. J. P. Attfield
Centre for Science at Extreme Conditions (CSEC) and School of Chemistry
University of Edinburgh
Mayfield Road, Edinburgh EH9 3JZ (UK)
E-mail: j.p.attfield@ed.ac.uk
R. D. Stewart, Dr. J.-W. G. Bos
Institute of Chemical Sciences and Centre for Advanced Energy Storage and Recovery
School of Engineering and Physical Sciences, Heriot-Watt University
Edinburgh EH14 4AS (UK)
Dr. W. Kockelmann
ISIS, Rutherford Appleton Laboratory
Oxon OX11 0QX (UK)

[**] We acknowledge support from EPSRC, STFC, the Leverhulme Trust, and the Royal Society.

Supporting Information for this article is available on the WWW under http://dx.doi.org/10.1002/anie.201403223.

by heating at 1200 °C for 15 min at a pressure of 10 GPa for Ln = Pr, Nd, and Sm, and 11 GPa for Ln = Eu, Gd, Tb, Dy, Ho, and Y. A stoichiometric mixture of Ru, RuO_2, and dried Ln_2O_3 (ca. 30 mg) was loaded into a platinum capsule and heated under pressure in a Walker-type module using a 14/8 cell configuration.

Powder X-ray diffraction patterns (Figure 1) show that Ln = La to Tb samples contain the $LnRuO_3$ perovskite with small amounts of residual RuO_2 and Ru as secondary phases. An increasing amount of the $Ln_2Ru_2O_7$ pyrochlore phase is seen for the smallest cations (with Ln = Dy, Ho, and Y), although a trace of the perovskite phase is still evident for Ln = Y. Hence, the $LnRuO_3$ perovskites follow the coordination rule that increasingly high pressures are required to stabilize a given structure as cation size decreases. $LnRuO_3$ perovskites of the smallest Ln = Er–Lu cations may be accessible at pressures in excess of 11 GPa. The synthesis of $CeRuO_3$ was also attempted, but gave mixtures containing CeO_2 with no perovskite-type phase evident.

Rietveld powder data fitting analysis to the powder X-ray diffraction patterns showed that all the $LnRuO_3$ perovskites adopt the orthorhombic *Pnma* superstructure at ambient conditions. This has a $\sqrt{2} \times 2 \times \sqrt{2}$ perovskite supercell structure owing to the ordered tilts of RuO_6 octahedra. The refined lattice parameters of the $LnRuO_3$ series are shown in Figure 2. The orthorhombic distortion (as shown by the difference between cell parameters *a* and *c*) decreases markedly for the largest cation (Ln = La), suggesting that $LaRuO_3$ may undergo a structural transition to a higher symmetry perovskite superstructure at high temperatures. This transition would be in keeping with other perovskite series, such as $LnNiO_3$, where *Pnma* symmetry changes to $R\bar{3}c$ for $LaNiO_3$.[20]

Neutron powder diffraction was used to obtain precise structure refinements of $LnRuO_3$ perovskites for Ln = La, Pr, and Nd. Data were collected from the GEM diffractometer at the ISIS facility for temperatures between 7 and 300 K, but no further structural distortions or magnetic ordering transitions were observed. The neutron diffraction data were used to investigate possible non-stoichiometry of the $LnRuO_3$ perovskites. Rietveld refinements (Figure 3 and Table 1)

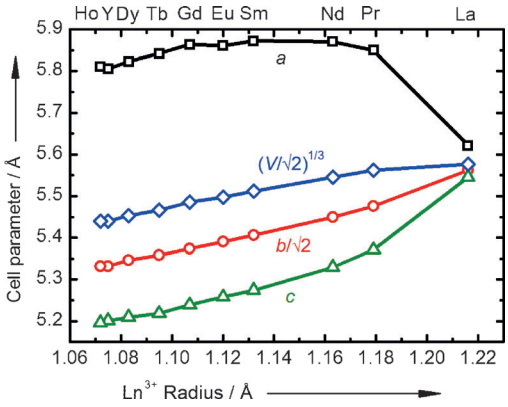

Figure 2. Refined lattice parameters (*a*, *b*, *c*) and unit cell volume *V* (as $(V/\sqrt{2})^{1/3}$) plotted against the Ln^{3+} ionic radius for $LnRuO_3$ perovskites. Errors bars are smaller than the data points.

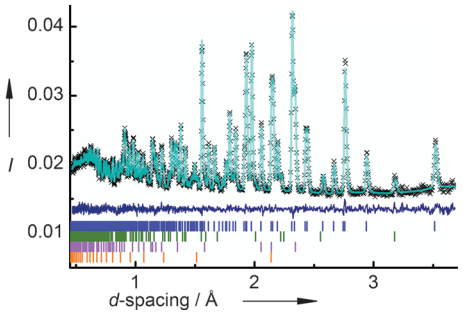

Figure 3. Rietveld powder data fitting analysis to neutron diffraction data for a $NdRuO_3$ sample (170 mg) at 300 K (weighted-profile residual R_{wp} = 1.7%). Reflection markers from top to bottom correspond to $NdRuO_3$, traces of RuO_2 and Ru, and the vanadium sample container.

Table 1: Refined structural parameters for $LnRuO_3$ perovskites (Ln = La, Pr, and Nd) at 300 K from neutron powder diffraction refinement.

Parameter	$LaRuO_3$	$PrRuO_3$	$NdRuO_3$
a [Å]	5.6214(2)	5.8577(3)	5.8774(3)
b [Å]	7.8663(2)	7.7460(4)	7.7064(4)
c [Å]	5.5462(2)	5.3726(3)	5.3291(2)
V [Å^3]	245.25(2)	243.78(3)	241.37(3)
Ln *Occ*	0.909(2)	1.0	1.0
Ln *x*	0.0428(2)	0.0697(6)	0.0745(3)
Ln *z*	0.0098(3)	0.9760(8)	0.9755(4)
Ln U_{iso} [Å^2]	1.15(3)	1.19(13)	0.92(6)
Ru *Occ*	0.931(2)	0.923(7)	0.886(6)
Ru U_{iso} [Å^2]	0.27(2)	0.42(12)	0.35(6)
O(1) *x*	0.2945(2)	0.3035(4)	0.3043(3)
O(1) *y*	0.4578(2)	0.0483(3)	0.0503(2)
O(1) *z*	0.4578(2)	0.6856(4)	0.6845(4)
O(1) U_{iso} [Å^2]	0.90(2)	0.79(10)	0.86(5)
O(2) *x*	0.4834(3)	0.4685(5)	0.4674(5)
O(2) *z*	0.9182(3)	0.0968(5)	0.1011(5)
O(2) U_{iso} [Å^2]	0.94(2)	0.79(12)	1.06(8)

showed that the oxygen sites are fully occupied, however, Ru sites have 7–11% vacancies in all three structures. Refinement of the Ln site occupancies showed 9% vacancies in $LaRuO_3$ but no significant vacancy concentration for Ln = Pr and Nd, so these occupancies were fixed at 100% in the final refinements in Table 1.

The neutron refinements show significant levels of cation vacancies and the refined compositions for the perovskite phases are $La_{0.91}Ru^{3.52+}{}_{0.93}O_3$, $PrRu^{3.26+}{}_{0.92}O_3$, and $NdRu^{3.37+}{}_{0.89}O_3$, showing that these materials have mixed Ru^{3+}/Ru^{4+} states with an average ruthenium oxidation state in the range +3.3 to +3.5. Occupancies from X-ray Rietveld powder fitting refinements are less precise but gave approximately 10% Ru vacancies in all of the $LnRuO_3$ samples, in agreement with the neutron refinements. The ruthenium states, calculated from Ru–O bond lengths using a standard bond-valence sum method,[21] were +3.3 in all three structures, and hence are consistent with the refined compositions.

The formation of cation vacancies evidences an oxidation mechanism, for example, non-stoichiometric $SrRu_{1-x}O_3$ is formed after heating $SrRuO_3$ perovskite at high oxygen pressures.[22] To investigate the range of non-stoichiometry in $LnRuO_3$ materials, samples with a starting composition $NdRu_{1-x}O_3$ where $x = 0$–0.25, corresponding to ruthenium oxidation states between +3 and +4, were prepared under the same reaction conditions (1200 °C and 10 GPa). However, the products contained increasing amounts of RuO_2 as x increases, the refined Ru-site occupancy of the perovskite phase was always near 90 %, and the lattice parameters and volume had no systematic variation with x, as shown in Figure 4. Hence we conclude that the

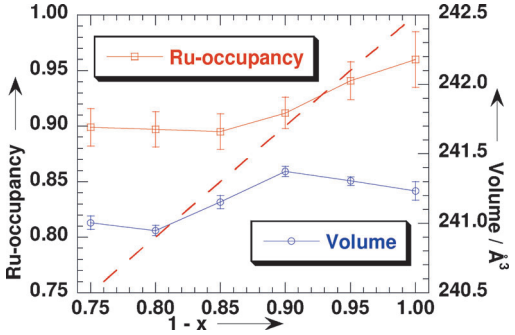

Figure 4. X-ray data refined Ru-site occupancies and unit cell volumes for the perovskite phase in samples with starting composition $NdRu_{1-x}O_3$ ($x = 0$–0.25). Broken line: expected occupancy variation based on the nominal composition.

range of non-stoichiometry is no more than a few percent and that the composition of the high-pressure perovskites is close to $LnRu_{0.9}O_3$ under the synthetic conditions used. Thus the ruthenium state is close to +3, although some Ru^{4+} is also present. Further phase-diagram studies are necessary to discover how the non-stoichiometry of $LnRuO_3$ perovskites varies with pressure and temperature. The presence of additional La-site vacancies in $LaRuO_3$ probably reflects the ambient-pressure conditions used to synthesize this phase. High-pressure synthesis tends to eliminate vacancy defects as volume is minimized, so the presence of approximately 10 % Ru-site vacancies in $LnRuO_3$ perovskites made at 10–11 GPa is notable and highlights the tendency of Ru^{3+} in oxide environments to disproportionate to Ru^{4+} and Ru metal.

Thermal variations of the Ru–O bond lengths and Ru-O-Ru angles for $LaRuO_3$ and $NdRuO_3$ from the neutron diffraction study are given in Figure 5. These results show that the increasing lattice distortion on replacing La by smaller Nd is accommodated both by increased octahedral tilting (Ru-O-Ru angles decrease from 153 to 146°) and through deformation of the RuO_6 octahedra. The octahedra are quite regular in $LaRuO_3$, where the three pairs of inequivalent Ru–O bonds all have bond lengths of 2.02–2.04 Å. However, a pronounced tetragonal compression that increases on cooling is observed for $NdRuO_3$ with two short (2.01 Å) and four long (2.07–2.08 Å) bonds.

Jahn–Teller distortion of octahedrally coordinated, low-spin $4d^5$ ruthenium(III) centers leads to tetragonal elongation, so the observed tetragonal compression parallel to the

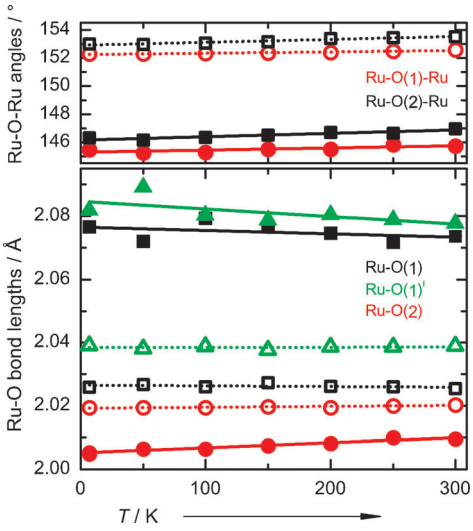

Figure 5. Thermal variations of Ru-O-Ru bond angles and Ru–O bond lengths (Ru–O(1) in the *ac* plane, Ru–O(2) along the *b*-axis) for $LaRuO_3$ (open symbols and broken lines) and $NdRuO_3$ (filled symbols and full lines), showing the octahedral compression of $NdRuO_3$.

b-axis is not consistent with orbital ordering. The lack of orbital order is also in keeping with the $c < b/\sqrt{2} < a$ relative magnitude of the cell parameters of all the $LnRuO_3$ perovskites (Figure 2) which is indicative of the normal O structure of *Pnma* perovskites. Octahedral compression is, however, consistent with significant spin-orbit coupling, and is further supported by physical-property measurements (see below).

Four-probe electrical resistivities of ceramic pellets were measured at 7–300 K for selected $LnRuO_3$ materials. All samples were found to be nonmetallic and the data (Figure 6a) follow Arrhenius behavior in the 50–300 K range with activation energies of 22 meV for $NdRuO_3$ and 41 meV for $GdRuO_3$, demonstrating that the $LnRuO_3$ perovskites are narrow band gap semiconductors.

Magnetic susceptibilities of $LnRuO_3$ samples in Figure 6b were measured at 2–300 K in a 1 T field using a SQUID magnetometer. All samples were found to be paramagnetic down to 2 K with no evidence of spin-ordering transitions, in agreement with the absence of magnetic diffraction peaks in the 7 K neutron diffraction patterns of the Ln = La, Pr, and Nd samples. Low-temperature anomalies are observed for the Ln = Pr, Nd, Sm, and Eu samples, as is evident in the inverse susceptibility plot for $NdRuO_3$ in Figure 6b, but these are close to the reported transitions of the corresponding $Ln_2Ru_2O_7$ pyrochlores and so are assigned to small traces of these phases, below the limit of detection by X-ray diffraction.[23,24]

Inverse susceptibilities were fitted using the expression $\chi^{-1} = [C/(T-\theta) + \chi_0]^{-1}$; the constant term χ_0 is required to fit a slight curvature of χ^{-1} as shown for $NdRuO_3$ in Figure 6b. The Weiss constant, θ, takes negative values for the early Ln = La, Pr, and Nd, but was found to be insignificant for the later lanthanides and was fixed at zero. The equation was fitted to the data for all the $LnRuO_3$ samples (Ln = La–Tb) with the exception of Ln = Eu, where temperature variation

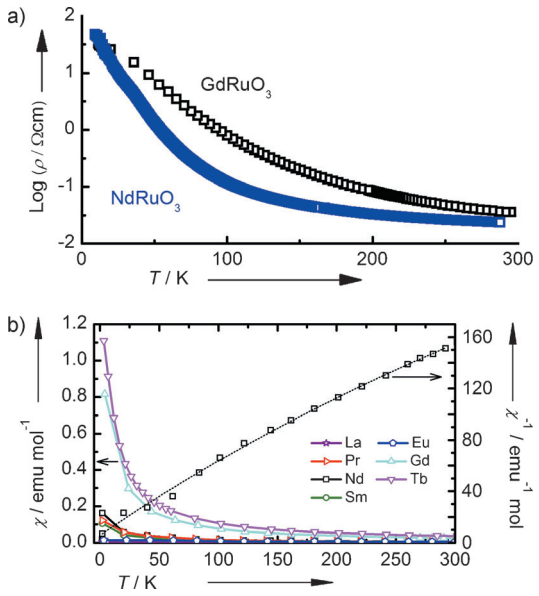

Figure 6. Variable-temperature property measurements for $LnRuO_3$ materials: a) plot of $\log_{10}$(resistivity) versus temperature (7–300 K) for $NdRuO_3$ and $GdRuO_3$ pellets; b) magnetic susceptibilities for $LnRuO_3$ and fitted inverse susceptibility versus temperature (2–300 K) for $NdRuO_3$.

of the effective moment precluded a useful fit. Values of the fitted magnetic parameters are shown in Table 2.

The magnetic properties of the $LaRuO_3$ sample appear to differ significantly from those of the other $LnRuO_3$ perovskites. The $LaRuO_3$ sample has a μ_{eff} value consistent with a mixture of localized $S = {}^1/_2$ ruthenium(III) and $S = 1$ ruthenium(IV) spins, with strong antiferromagnetic exchange interactions resulting in a large negative Weiss constant. The absence of a long-range ordering transition most likely reflects disorder caused by cation-site vacancies and mixed Ru^{3+}/Ru^{4+} states following the neutron-analyzed composition $La_{0.91}Ru^{3.52+}{}_{0.93}O_3$. Estimation of the ruthenium moment is more difficult for the other $LnRuO_3$ perovskites containing magnetic Ln^{3+} cations. However, the experimental effective moments for the $LnRuO_3$ materials where Ln = Pr, Nd, Sm, Gd, and Tb are all close to the ideal Ln^{3+} values, so any contribution from a paramagnetic ruthenium moment is small (at most approximately 0.8 μ_B for $SmRuO_3$). These materials have small or zero Weiss constants and significant temperature-independent susceptibilities ($\chi_0 \approx 10^{-3}$ emu mol^{-1}). This can be indicative of Pauli paramagnetism in metallic systems, but is also consistent with strong spin-orbit coupling in Mott insulators.[25] Europium(III) has a $J = 0$ ground state and the effective moment often shows a strong temperature dependence as thermally excited states become populated. The effective moment of 3.2–3.9 μ_B observed at 150–300 K for $EuRuO_3$ is typical of $4f^6$ Eu^{3+} materials, whereas $4f^7$ Eu^{2+} would have a large, temperature-independent moment of approximately 7.9 μ_B. This observation, in combination with the smooth trend of lattice parameters in Figure 2, confirms that the charge distribution in this material (neglecting vacancies) is $Eu^{3+}Ru^{3+}O_3$ rather than the alternative ground state $Eu^{2+}Ru^{4+}O_3$.

Strong spin-orbit coupling effects in heavy transition-metal oxides, notably iridium oxides based on low-spin d^5 Ir^{4+}, are of interest as they can convert these systems from correlated-metal states into topological Mott insulator states.[26] The strong spin-orbit coupling effect is also suggested by the combination of tetragonal octahedral compression, a narrow band-gap semiconducting behavior, and small effective-moment Curie–Weiss paramagnetism with an additional constant term, as observed for the high-pressure $LnRuO_3$ materials based on low-spin d^5 Ru^{3+}. Disorder created by cation deficiency may also contribute to the insulating behavior.

In conclusion, an extensive series of new $LnRuO_3$ perovskites has been synthesized at high pressure, although $LaRuO_3$ is accessible at ambient pressure. These Ru^{III}-based oxides are ruthenium deficient and high-pressure samples have compositions close to $LnRu_{0.9}O_3$. While perovskite-related oxides are often used to stabilize high oxidation states of transition metals,[27] such as +4 to +6 for ruthenium, our results and the recently reported $SrFe_{0.5}Ru_{0.5}O_2$[15] show that Ru^{2+} and Ru^{3+} can also be isolated in perovskites. The $LnRuO_3$ materials adopt an orthorhombic *Pnma* perovskite superstructure with tetragonal compression of the RuO_6 octahedra. This distortion, and the observed narrow band-gap semiconductivity and small effective-moment Curie–Weiss paramagnetism, are consistent with Mott insulator behavior, driven by a combination of strong spin-orbit coupling and disorder.

Table 2: Fitted magnetic parameters for $LnRuO_3$ samples and derived moments.[a]

Ln	θ [K]	C [emu K mol^{-1}]	μ_{eff} [μ_B]	$\mu_{eff}(Ln^{3+})$ [μ_B]	χ_0 [emu mol^{-1}]
La	−119(5)	0.52(2)	2.04	0	0.0006(1)
Pr	−8.8(8)	1.71(2)	3.69	3.58	0.0001(1)
Nd	−9(3)	1.56(8)	3.53	3.62	0.0014(2)
Sm	0	0.162(3)	1.14	0.85	0.0015(1)
Eu	–	–	3.2–3.9	0	–
Gd	0	7.68(7)	7.84	7.94	0.0007(3)
Tb	0	10.1(1)	8.97	9.72	0.0027(5)

[a] Effective magnetic moments were obtained from the Curie constants as $\sqrt{8C}$, except for Ln = Eu where the range of values is from $\sqrt{8\chi T}$ between 150 and 300 K. Calculated ground J-state Ln^{3+} moments are also shown.

Received: March 12, 2014
Published online: June 24, 2014

Keywords: oxides · perovskites · ruthenium · spin-orbit coupling · X-ray diffraction

[1] R. J. Cava, *Dalton Trans.* **2004**, 2979–2987.
[2] S. A. Grigera, R. S. Perry, A. J. Schofield, M. Chiao, S. R. Julian, G. G. Lonzarich, S. I. Ikeda, Y. Maeno, A. J. Millis, A. P. Mackenzie, *Science* **2001**, *294*, 329–332.
[3] Y. Maeno, H. Hashimoto, K. Yoshida, S. Nishizaki, T. Fujita, J. G. Bednorz, F. Lichtenberg, *Nature* **1994**, *372*, 532–534.
[4] J. M. Longo, *J. Appl. Phys.* **1968**, *39*, 1327–1328.
[5] G. Cao, S. McCall, M. Shepard, J. E. Crow, R. P. Guertin, *Phys. Rev. B* **1997**, *56*, R2916–R2919.

[6] C.-Q. Jin et al., *Proc. Natl. Acad. Sci.* **2008**, *105*, 7115 – 7119.
[7] S. A. J. Kimber, J. A. Rodgers, H. Wu, C. A. Murray, D. N. Argyriou, A. N. Fitch, D. I. Khomskii, J. P. Attfield, *Phys. Rev. Lett.* **2009**, *102*, 046409.
[8] R. Aléonard, E. F. Bertaut, M. C. Montmory, R. Pauthenet, *J. Appl. Phys.* **1962**, *33*, 1205.
[9] S. J. Makowski, J. A. Rodgers, P. F. Henry, J. P. Attfield, J.-W. G. Bos, *Chem. Mater.* **2009**, *21*, 264 – 272.
[10] A. C. McLaughlin, J. P. Attfield, *Phys. Rev. B* **2003**, *68*, 014503.
[11] D. Mandrus, J. Thompson, R. Gaal, L. Forro, J. Bryan, B. Chakoumakos, L. Woods, B. Sales, R. Fishman, V. Keppens, *Phys. Rev. B* **2001**, *63*, 195104.
[12] W. Klein, R. K. Kremer, M. Jansen, *J. Mater. Chem.* **2007**, *17*, 1356 – 1360.
[13] S. A. J. Kimber, M. S. Senn, S. Fratini, H. Wu, A. H. Hill, P. Manuel, J. P. Attfield, D. N. Argyriou, P. F. Henry, *Phys. Rev. Lett.* **2012**, *108*, 217205.
[14] M. D. Silverman, H. A. Levy, *J. Am. Chem. Soc.* **1954**, *76*, 3317 – 3319.
[15] F. D. Romero, S. J. Burr, J. E. McGrady, D. Gianolio, G. Cibin, M. A. Hayward, *J. Am. Chem. Soc.* **2013**, *135*, 1838 – 1844.
[16] R. J. Bouchard, J. F. Weiher, *J. Solid State Chem.* **1972**, *4*, 80 – 86.
[17] N. K. Labhsetwar, A. Watanabe, T. Mitsuhashi, *Appl. Catal. B* **2003**, *40*, 21 – 30.
[18] R. Greatrex, G. Hu, D. C. Munro, *Mater. Res. Bull.* **1986**, *21*, 797 – 802.
[19] H. Kobayashi, M. Nagata, R. Kanno, Y. Kawamoto, *Mater. Res. Bull.* **1994**, *29*, 1271 – 1280.
[20] J. A. Alonso, M. J. Martínez-Lope, M. T. Casais, M. T. Fernández-Díaz, *Inorg. Chem.* **2000**, *39*, 917 – 923.
[21] N. E. Brese, M. O'Keffe, *Acta Crystallogr. Sect. B* **1991**, *47*, 192 – 197.
[22] B. Dabrowski, O. Chmaissem, P. Klamut, S. Kolesnik, M. Maxwell, J. Mais, Y. Ito, B. Armstrong, J. Jorgensen, S. Short, *Phys. Rev. B* **2004**, *70*, 014423.
[23] W. D. Ryden, A. W. Lawson, *J. Chem. Phys.* **1970**, *52*, 6058 – 6061.
[24] N. Taira, M. Wakeshima, Y. Hinatsu, *J. Phys. Condens. Matter* **1999**, *11*, 6983 – 6990.
[25] A. S. Erickson, S. Misra, G. J. Miller, R. R. Gupta, Z. Schlesinger, W. A. Harrison, J. M. Kim, I. R. Fisher, *Phys. Rev. Lett.* **2007**, *99*, 016404.
[26] D. Pesin, L. Balents, *Nat. Phys.* **2010**, *6*, 376 – 381.
[27] J. P. Attfield, G. Ferey, *J. Solid State Chem.* **1989**, *80*, 112 – 119.

